



This is a repository copy of *Synthesis of zirconolite-2M ceramics for immobilisation of neptunium*.

White Rose Research Online URL for this paper:
<https://eprints.whiterose.ac.uk/164800/>

Version: Accepted Version

Article:

Wei, Z-J, Bao, W.-C., Sun, S.-K. et al. (7 more authors) (2021) Synthesis of zirconolite-2M ceramics for immobilisation of neptunium. *Ceramics International*, 47 (1). pp. 1047-1052. ISSN 0272-8842

<https://doi.org/10.1016/j.ceramint.2020.08.220>

Article available under the terms of the CC-BY-NC-ND licence
(<https://creativecommons.org/licenses/by-nc-nd/4.0/>).

Reuse

This article is distributed under the terms of the Creative Commons Attribution-NonCommercial-NoDerivs (CC BY-NC-ND) licence. This licence only allows you to download this work and share it with others as long as you credit the authors, but you can't change the article in any way or use it commercially. More information and the full terms of the licence here: <https://creativecommons.org/licenses/>

Takedown

If you consider content in White Rose Research Online to be in breach of UK law, please notify us by emailing eprints@whiterose.ac.uk including the URL of the record and the reason for the withdrawal request.



eprints@whiterose.ac.uk
<https://eprints.whiterose.ac.uk/>

Synthesis of zirconolite-2M ceramics for immobilisation of neptunium

Zi-Jun Wei^{a*}, Wei-Chao Bao^{b*}, Shi-Kuan Sun^{c#}, Lewis R. Blackburn^c, Sheng-Heng Tan^d, Laura J. Gardner^c, Wei-Ming Guo^{a#}, Fangfang Xu^b, Neil C. Hyatt^c, Hua-Tay Lin^a

^a*School of Electromechanical Engineering, Guangdong University of Technology, Guangzhou 510006, China*

^b*The State Key Laboratory of High Performance Ceramics and Superfine Microstructure, Shanghai Institute of Ceramics, Chinese Academy of Sciences, Shanghai 200050, China*

^c*Immobilisation Science Laboratory, Department of Materials Science and Engineering, University of Sheffield, Mappin Street, S1 3JD, UK*

^d*Department of Radiochemistry, China Institute of Atomic Energy, Beijing 102413, China*

* - These authors contributed equally to this paper;

- Corresponding author. Email: shikuan.sun@sheffield.ac.uk (S.-K. Sun), guo1238@126.com (W.-M. Guo)

Abstract

Praseodymium-doped zirconolite ceramics targeting nominal composition $\text{Ca}_{1-x}\text{Pr}_x\text{ZrTi}_{2-5x/3}\text{Al}_{5x/3}\text{O}_7$ ($x \leq 0.20$, $\Delta x = 0.05$) were fabricated by a mixed oxide solid state reaction, at 1350 °C in air for 20 h. Praseodymium (Pr) was employed as a surrogate for neptunium (Np), with Al^{3+} co-accommodated to provide charge balance. High-resolution transmission electron microscopy and electron diffraction analyses confirmed that zirconolite crystallised as the 2M monoclinic polytype throughout the phase evolution, with no evidence of transformation to other polytype structures. Phase assemblage and microstructural data were consistent with zirconolite occupying a high fraction of the phase assemblage ($> ca. 93 \text{ wt. } \%$), alongside a minor secondary perovskite phase at all levels of targeted Pr incorporation. Despite this, it was demonstrated near theoretical density formed through a solid-state fabrication route, and we therefore propose that, through analogy with the corresponding Pr solid solution, zirconolite may be a suitable candidate for the immobilisation of Np-bearing wastes.

Keywords: Zirconolite; Immobilisation; Neptunium; Polytype; Surrogate.

1 Introduction

The effective management and disposition of minor actinide species (MA) such as ^{237}Np and ^{241}Am , derived from reprocessing spent nuclear fuel (SNF) [1], requires the development of refractory wasteforms with high aqueous durability [2,3]. Of these, ^{237}Np is of particular importance due to its extremely long half-life and large quantities ($t_{1/2} = 2.1 \times 10^6$ y; ~ 0.04 wt.% in PWR spent nuclear fuel; the specific activity is 26 Bq/ μg), providing a significant contribution to the overall radiogenic waste output in the disposal environment [4]. Wasteforms previously proposed for Np include bitumen, borosilicate glass and zirconia [5-7]. The chemical immobilisation of Np may best be achieved through accommodation in solid solution with a suitably durable ceramic material, such as the titanate phases utilised in the Synroc mineral assemblage, which exhibit superior aqueous durability with respect to vitrified wasteforms, providing extensive isolation from the biosphere over geological timescales [8-10].

As an attractive ceramic wasteform, zirconolite (nominally $\text{CaZrTi}_2\text{O}_7$) has demonstrated compositional flexibility [11,12], exceptional chemical stability [13], and high radiation tolerance [14]. Zirconolite has demonstrated affinity for the incorporation of actinide species in solid solution, such as U [15], Np [16,17] and Pu [16,17] with moderate to high waste loading, although depending on the solid solution regime, this may be accommodated by polytypical transition. Considering Np, the incorporation of tetravalent Np^{4+} within the Ca^{2+} site in zirconolite was reported by Begg *et al.* with the formation of a near-single phase $\text{Ca}_{0.8}\text{Np}_{0.2}\text{ZrTi}_{1.6}\text{Al}_{0.4}\text{O}_7$, although no comments were made with respect to the zirconolite crystal structure, either by powder X-ray diffraction or electron diffraction [16,17]. Therefore, it remains unclear whether the incorporation of Np^{4+} within the zirconolite structure resulted in a polymorphic transition to either the zirconolite-4M or 3T structures. Furthermore, these materials were fabricated by sol-gel route, by which a liquid mixture of alkoxides and nitrates were stirred until dry and calcined prior to solid state sintering [18]. A solid state reaction from constituent oxide precursors is considered a preferable immobilisation route, as the process is straightforward with proven scalability, with minimal secondary contamination from handling of liquid phases.

Praseodymium (Pr) is considered a suitable surrogate for Np on the basis of cost and expediency [19], with both elements exhibiting comparable ionic radii in 8-fold coordination ($\text{Pr}^{4+} = 0.96 \text{ \AA}$, $\text{Np}^{4+} = 0.98 \text{ \AA}$) [20], the Pr_6O_{11} ($\text{Pr}_2^{3+}\text{Pr}_4^{4+}\text{O}_{11}$) precursor contains mixed oxidation states in the ratio $\text{Pr}^{3+} : \text{Pr}^{4+} = 1 : 2$. In the present work, we report the incorporation of Pr as a representative surrogate for Np, within zirconolite targeting $\text{Ca}_{1-x}\text{Pr}_x\text{ZrTi}_{2-5x/3}\text{Al}_{5x/3}\text{O}_7$, whose solid solution is designed to accommodate $\text{Pr}^{3+} : \text{Pr}^{4+}$ at a 1:2 molar ratio within the Ca^{2+} site with Al_2O_3 to provide charge compensation. Therefore, the aim of this work was to determine the solubility of Pr

within the zirconolite structure utilizing a conventional solid state synthesis route from mixed oxide precursors, to provide insight into the phase assemblage and polytype assignment of the Np surrogate zirconolite wasteform.

2 Experimental Procedure

2.1 Materials Synthesis

Zirconolite ceramics targeting $\text{Ca}_{1-x}\text{Pr}_x\text{ZrTi}_{2.5x/3}\text{Al}_{5x/3}\text{O}_7$ ($x \leq 0.20$; $\Delta x = 0.05$) were prepared *via* solid state synthesis from constituent oxides CaTiO_3 (> 99.5% purity, Macklin Reagent Co., China), ZrO_2 (> 99.8% purity, Xili Grinding Tech. Co. Ltd., China), TiO_2 (anatase, > 99.5% purity, Macklin Reagent Co., China) Pr_6O_{11} (> 99.9% purity, Shanghai Aladdin Bio-chem Technology Co., Ltd., China) and Al_2O_3 (> 99.9% purity, Shanghai Aladdin Bio-chem Technology Co., Ltd., China). Precursors were batched according to desired compositions ($\text{Ca}_{1-x}\text{Pr}_x\text{ZrTi}_{2.5x/3}\text{Al}_{5x/3}\text{O}_7$, $x \leq 0.20$, $\Delta x = 0.05$) and homogenised by roller milling with ZrO_2 media for 24 h, with acetone added as a milling agent. After drying, the milled precursor material was pressed into the walls of a stainless steel die (20 mm diameter) and compressed under ~ 100 MPa uniaxial pressure. Pellets were placed into a furnace and sintered in air at 1350 °C, for a dwell time of 20 h.

2.2 Materials Characterization

Reacted pellets were finely ground and analysed by powder X-ray diffraction (powder-XRD) using a Bruker Advance D8 diffractometer (Cu-K α , $\lambda = 1.5418 \text{ \AA}$); diffraction data were acquired in the 2θ range of $10^\circ \sim 80^\circ$, with step size of 0.02° and 1 s per step. Refinement of powder XRD data was performed using the Rietveld method, allowing calculation of the zirconolite unit cell parameters and relative weight fraction of accompanying phases, using the GSAS package with EXPGUI interface ^[21]. Selected area electron diffraction data (SAED) and high-resolution transmission electron microscope (HRTEM) images were acquired on the crushed grain from specimens of $x = 0.05$ and 0.15 using a FEI Tecnai G2 F20 transmission electron microscope. The density of the sintered pellets was measured by the Archimedes method using deionised water as the medium. The sintered pellets were polished to a $1.0 \mu\text{m}$ finish and thermal etched at 1200 °C for 2 h in air prior to microstructure observation. Backscattered electrons (BSE) images of pellet surfaces were collected using a FEI 430 Nova NanoSEM scanning electron microscope (SEM), equipped with a X-MarN (Oxford Instruments) for energy dispersive X-ray spectroscopy (EDS) analysis. In order to determine the average composition of the zirconolite phase, 10 EDS measurements were taken from spatially distributed areas for each sample. A powdered aliquot for

each composition was prepared for X-ray photoelectron spectroscopy (XPS) using a K-Alpha X-ray Photoelectron Spectrometer system (ThermoFischer Scientific) operating at $10^{-8} - 10^{-9}$ Torr, by finely spreading on adhesive carbon tape, together with a Pr_6O_{11} reference compound. A monochromated Al $K\alpha$ source was used (1486.7 eV) with peaks referenced to a carbon C 1s peak (284.6 eV).

3 Results and Discussion

Powder XRD data for each composition is displayed in **Fig. 1**, with the major phase clearly identified as zirconolite-2M (prototypically $\text{CaZrTi}_2\text{O}_7$, space group $C2/c$, ICSD: 190015 [22]) at all targeted levels of Pr concentration. No ancillary reflections attributed to Pr_6O_{11} , Pr_2O_3 or Al_2O_3 were detected, indicating Pr and Al were successfully incorporated within the zirconolite-2M structure throughout the solid solution range. Polymorphic transformations from zirconolite-2M to zirconolite-4M or zirconolite-3O have been previously reported for closely related systems; $\text{Ca}_{1-x}\text{Zr}_{1-x}\text{Nd}_x\text{Ti}_2\text{O}_7$ [23], $\text{CaZr}_{1-x}\text{Ce}_x\text{Ti}_2\text{O}_7$ [24], $\text{CaZr}_{1-x}\text{U}_x\text{Ti}_2\text{O}_7$ [11] and $\text{Ca}_{1-x}\text{Gd}_x\text{ZrTi}_{2-x}(\text{Fe,Al})_x\text{O}_7$ [25], however in the present work, powder XRD data were consistent with zirconolite adopting the 2M polytype throughout the phase evolution, as compared with Bragg position of zirconolite-2M (black vertical lines in the bottom of **Fig. 1**) and its theoretical intensities (green vertical lines). A minor perovskite phase (nominally CaTiO_3 , ICSD: 183209) was detected by the prominent reflection at $2\theta = 33.1^\circ$ at all levels of targeted Pr incorporation ($0.05 \leq x \leq 0.20$). Furthermore, the relative intensity of the perovskite reflections appeared to increase as a function of (x). Quantitative phase analysis, produced from Rietveld refinement of powder XRD data was collected and displayed in **Table 1**. When targeting $x = 0.05$, the phase assemblage was comprised of 97.04 ± 0.05 wt. % zirconolite-2M and 2.96 ± 0.48 wt. % perovskite. The relative overall occupation of the zirconolite-2M phase was observed to decrease to 93.19 ± 0.12 wt. % when the composition targeted $x = 0.20$. The relative density of the sintered product for each composition is also listed in **Table 1**; the product density appeared to increase relative to the targeted Pr concentration, which may incur benefit with regards to volume reduction and incorporation rate.

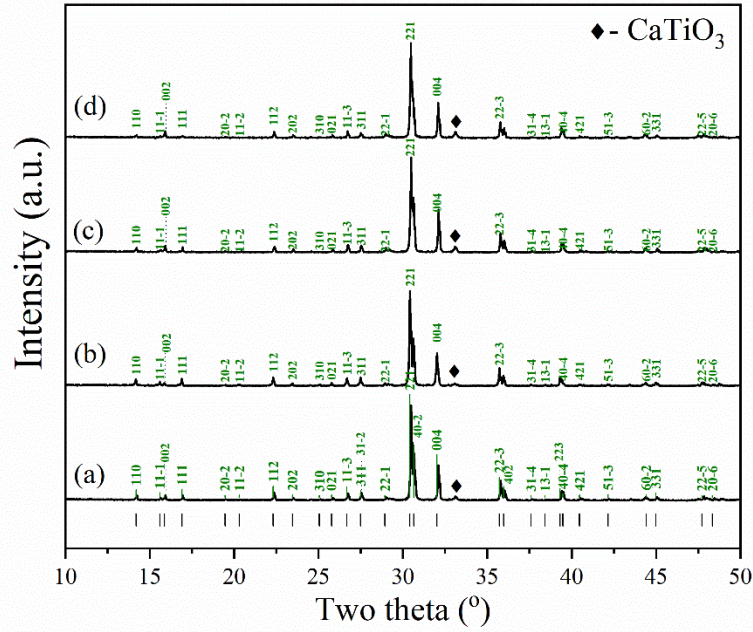


Fig. 1) Powder XRD data for $\text{Ca}_{1-x}\text{Pr}_x\text{ZrTi}_{2.5x/3}\text{Al}_{5x/3}\text{O}_7$ at $x =$ (a) 0.05 , (b) 0.10 , (c) 0.15 and (d) 0.20 compositions sintered in air at 1350 °C for 20 h. Green labels and black vertical lines are representative of the theoretical intensities and the Bragg positions of zirconolite-2M reflections (ICSD: 190015 [22]).

Table 1) Weight fraction of the zirconolite-2M phase and relative density of obtained product, alongside comparison of nominal and measured $\text{Ca}_{1-x}\text{Pr}_x\text{ZrTi}_{2.5x/3}\text{Al}_{5x/3}\text{O}_7$ compositions determined by EDS analysis.

- Data are calculated based on only cations and normalised.

Doping Level (x)	Zirconolite-2M Yield (wt. %)	Relative Density (%)	Atomic Ratio (at. %)	Ca	Pr	Zr	Ti	Al
			#					
0.05	97.04 ± 0.05	82.43 ± 0.07	Theoretical	23.75	1.25	25.00	47.92	2.08
			Measured	22.31 ± 0.18	1.74 ± 0.39	31.89 ± 0.37	40.32 ± 0.39	3.74 ± 0.14
0.10	95.37 ± 0.07	86.63 ± 0.03	Theoretical	22.50	2.50	25.00	45.83	4.17
			Measured	20.48 ± 0.19	3.23 ± 0.35	32.42 ± 0.47	39.92 ± 0.34	3.96 ± 0.18
0.15	94.29 ± 0.09	92.59 ± 0.11	Theoretical	21.25	3.75	25.00	43.75	6.25
			Measured	18.58 ± 0.32	5.10 ± 0.26	32.94 ± 0.48	37.38 ± 0.55	5.99 ± 0.16
0.20	93.19 ± 0.12	92.05 ± 0.03	Theoretical	20.00	5.00	25.00	41.67	8.33
			Measured	17.94 ± 0.21	6.61 ± 0.23	33.24 ± 0.56	35.44 ± 0.36	6.78 ± 0.17

Zirconolite intergrowth defects are a common artefact, resulting in variation of stacking sequence of adjacent HTB modular layers, manifesting in the formation of zirconolite polytypes such as 4M or 3T. The formation of zirconolite polytypes is dependent on the targeted solid solution regime and processing environment [24]. The incorporation of small concentrations of dopant atoms (such as REE³⁺ species) is often sufficient to promote complex intergrowth defects that not readily detected by powder XRD analysis. Selection Area Electron Diffraction (SAED) analysis is capable of detecting the signatures of stacking disorder; Vance *et al.* reported extensive streaking in zone axis diffraction data for zirconolite-4M [15]. In order to determine the polytype obtained throughout the phase evolution of Ca_{1-x}Pr_xZrTi_{2-5x/3}Al_{5x/3}O₇, SAED patterns were acquired for x = 0.05 and x = 0.15 (Fig. 2).

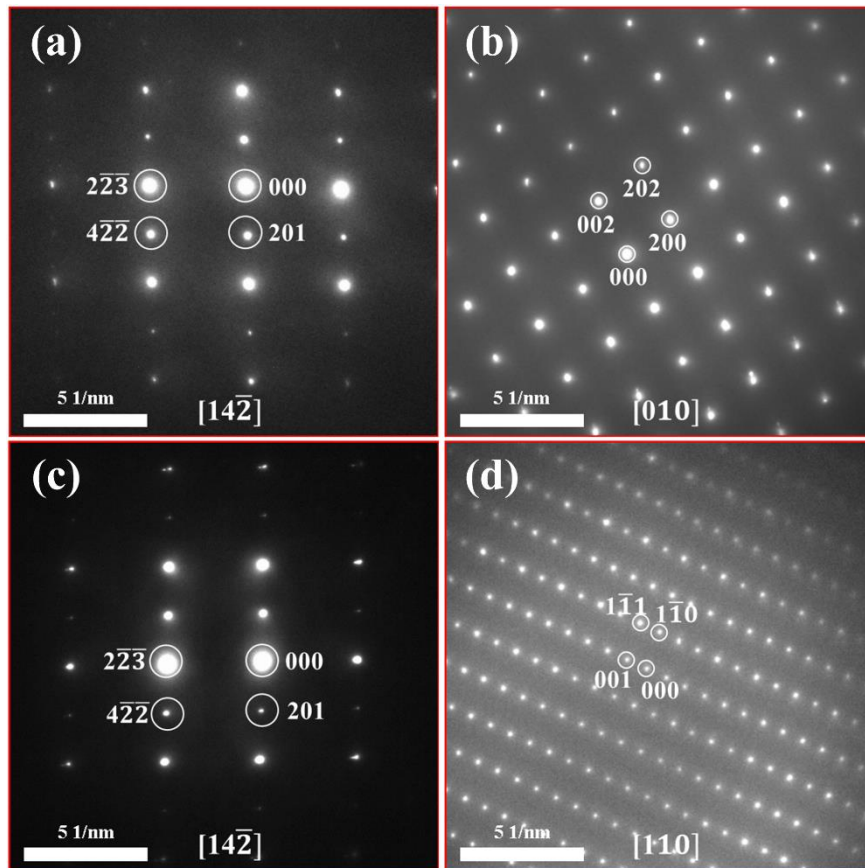


Fig. 2) SAED patterns for Ca_{1-x}Pr_xZrTi_{2-5x/3}Al_{5x/3}O₇ taken along the [14 $\bar{2}$] and [010] zone axis of x = 0.05 (Fig. 2a-b); [14 $\bar{2}$] and [110] zone axes of x = 0.15 (Fig. 2c-d).

Both data sets in Fig. 2 were absent of significant twinning or stacking disorder, exhibiting sharp, well-defined reflections. For both x = 0.05 and x = 0.15 compositions, the SAED data could only be indexed to the zirconolite-2M polytype (space group C2/c) confirming that no polytypical transformations occurred throughout the evolution of the solid solution. Depending on the synthesis method, zirconolite-2M may crystallise with extensive stacking

faults, for example in the case of Liao *et al.* in which zirconolite-2M was derived from a glass-matrix [26]. In order to investigate the nano-scale structure of $\text{Ca}_{1-x}\text{Pr}_x\text{ZrTi}_{2-5x/3}\text{Al}_{5x/3}\text{O}_7$ samples ($x = 0.05, x = 0.15$), were analysed by HRTEM (Fig. 3). Clear lattice fringes were visible, without major distortions or lattice defects, demonstrating $\text{Ca}_{1-x}\text{Pr}_x\text{ZrTi}_{2-5x/3}\text{Al}_{5x/3}\text{O}_7$ compositions were highly crystalline without obvious stacking faults. These data indicate that the atomic planes are well ordered as zirconolite-2M, consistent with powder XRD data.

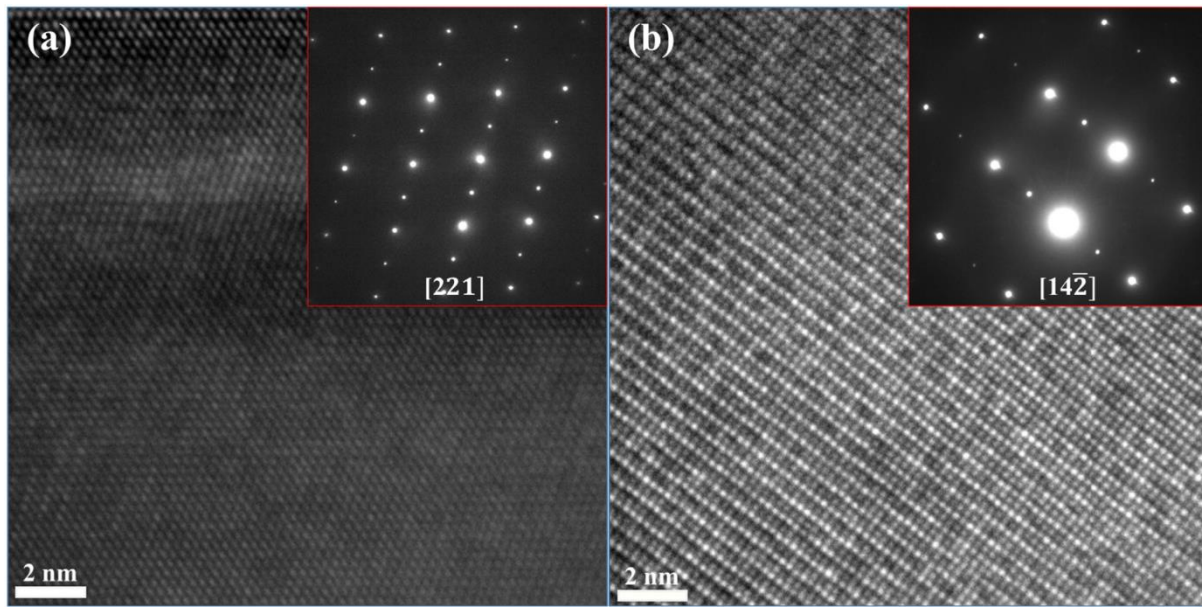


Fig. 3 HRTEM images of $\text{Ca}_{1-x}\text{Pr}_x\text{ZrTi}_{2-5x/3}\text{Al}_{5x/3}\text{O}_7$ with corresponding SAED at $x =$ (a) 0.05 and (b) 0.15.

Representative microstructures of $\text{Ca}_{1-x}\text{Pr}_x\text{ZrTi}_{2-5x/3}\text{Al}_{5x/3}\text{O}_7$ ceramics ($0.05 \leq x \leq 0.20$) are displayed in Fig. 4; despite minor visible porosity, the sintered ceramic specimens demonstrated a relatively dense morphology. A near homogeneous matrix of zirconolite-2M was observed by backscattered electron contrast, with minor inclusions of perovskite evidenced, as darker grains relative to the BSE contrast of the bulk (highlighted by red circles in Fig. 4). It was evident from close inspection of EDS data for the perovskite grains (Fig. 5) that Pr was incorporated in dilute solid solution with the CaTiO_3 phase, indicative of a secondary reaction product rather than unreacted precursor. This may be problematic for Np containing wastes, as synthesis under reducing conditions may promote the partial formation of Np^{3+} , and subsequent accommodation in the perovskite phase. The leaching rate of calcium in CaTiO_3 at 90°C under different pH levels was previously measured to be $6.30 \times 10^{-2} \text{ g}\cdot\text{m}^{-2}\cdot\text{d}^{-1}$ (pH = 2.1), $2.7 \times 10^{-1} \text{ g}\cdot\text{m}^{-2}\cdot\text{d}^{-1}$ (pH = 3.1) and $3.70 \times 10^{-2} \text{ g}\cdot\text{m}^{-2}\cdot\text{d}^{-1}$ (pH = 12.9) [27]. All of these values was much higher than Ca in $\text{CaZrTi}_2\text{O}_7$ (in the order of magnitude of $10^{-3} \text{ g}\cdot\text{m}^{-2}\cdot\text{d}^{-1}$ [27]). As CaTiO_3 has demonstrated lower aqueous durability than the target $\text{CaZrTi}_2\text{O}_7$ phase, the partial retention of the Np inventory in this manner may substantially reduce the overall wasteform performance, by promoting the premature release of Np from CaTiO_3 .

Further studies on optimal formulation by starting from the excessive amount of ZrO_2 and TiO_2 in the raw materials would be desirable to remove the perovskite phase.

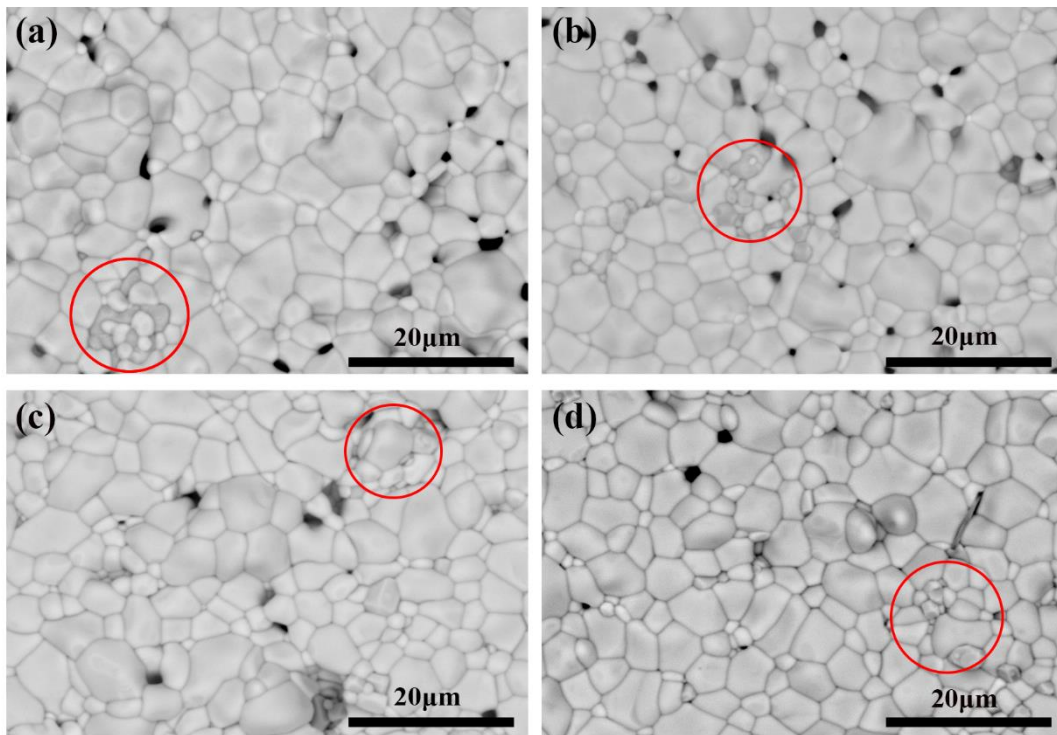


Fig. 4) Representative BSE micrographs of the $Ca_{1-x}Pr_xZrTi_{2.5x/3}Al_{5x/3}O_7$ ceramic microstructure at $x =$ (a) 0.05, (b) 0.10, (c) 0.15 and (d) 0.20, after sintering in air at 1350 °C for 20 h. Red circles highlight the $CaTiO_3$ phase. The black region in grain boundary is the porosity.

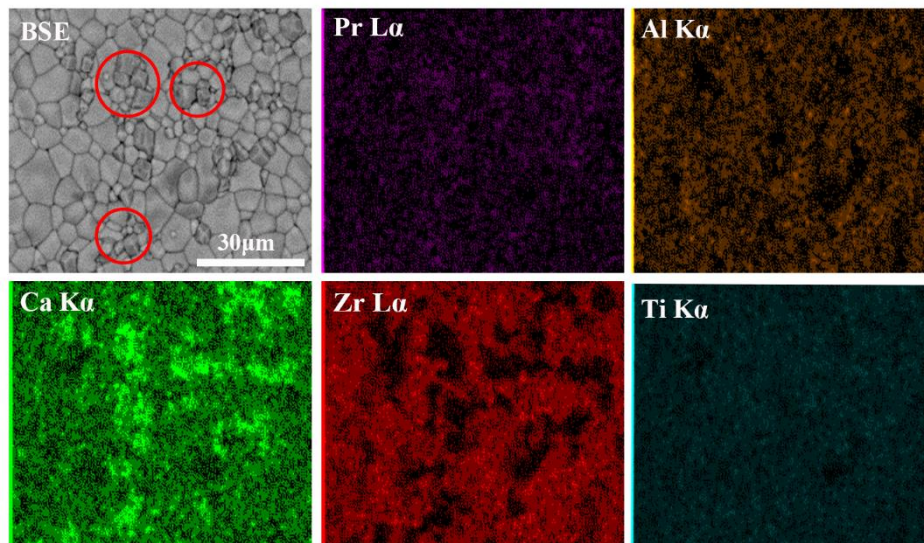


Fig. 5) Representative BSE micrograph and corresponding EDS data mapping for the $x = 0.20$ sample. The red circles highlight the $CaTiO_3$ phase.

The normalised composition of the zirconolite phase produced at each targeted concentration of Pr was determined by EDS spot analysis (**Table 1**). The atomic ratio of Pr and Al increased gradually as a function of the substitution level, indicative of successful incorporation within the target host phase. Surprisingly, the ratio of Zr was consistently elevated with respect to the nominal composition; however, this may be attributed to the presence of the perovskite phase, resulting in the deficiency of Ca and Ti in zirconolite. The sum of Ca and Pr remained near-constant throughout the phase evolution (~ 24 at. %), with similar trends observed for (Ti +Al).

In order to determine the oxidation state of Pr within the zirconolite host phase, samples were analysed using XPS (**Fig. 6**). The zirconolite spectra exhibited a line profile consistent with the Pr 3d_{5/2} spectra, consisting of two maxima separated by ~ 4.1 eV binding energy, with no visible shift observed. Comparison of zirconolite XPS spectra with the Pr₆O₁₁ standard indicated the oxidation state of Pr remained constant as the concentration of Pr increased from x = 0.10 to x = 0.20. Attempts were made to resolve the Pr 3d XPS data using component functions, however by reviewing the available literature for quantitative determination of Pr XPS spectra, no reliable calculations were available (unlike Ce 3d, for example) The fitting of Pr 3d core levels is difficult and remains controversial [28,29], as Pr₂O₃ and PrO₂ compounds both exhibit signals in the Pr 3d_{5/2} and 3d_{3/2} peak [30], hence it was not possible to exclude either Pr oxidation state in the sample, in particular for samples with dilute Pr content (ca. 8 wt. % for x = 0.20). X-ray absorption near edge structure (XANES) data would be desirable for future work [31-33] to elucidate the true oxidation state(s) for these compounds.

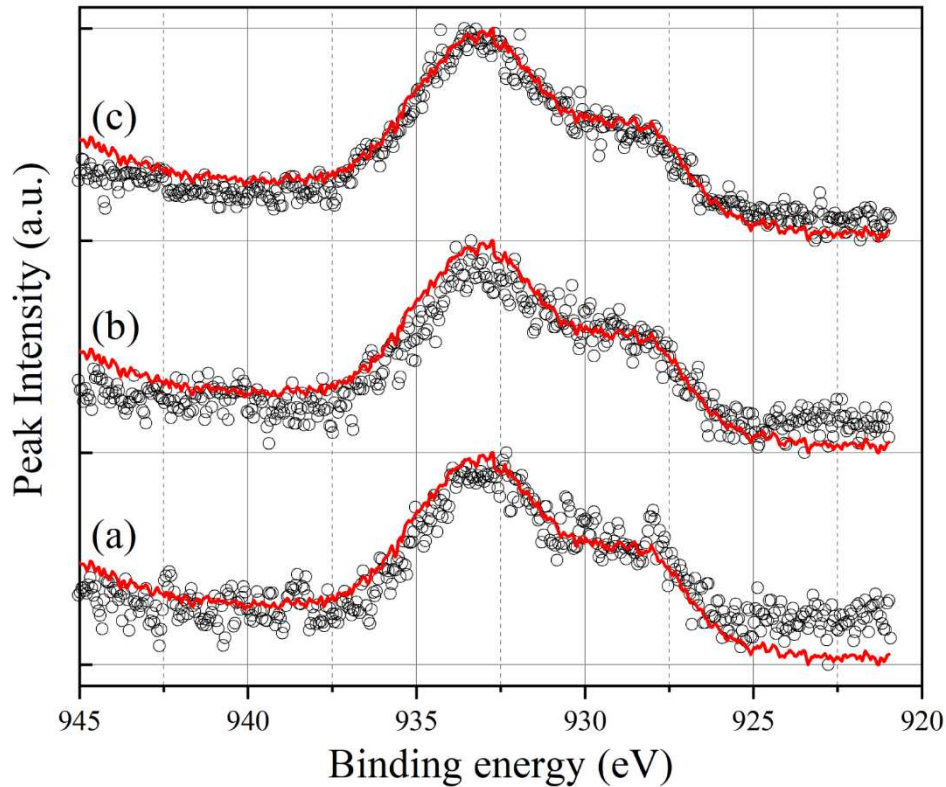


Fig. 6 XPS spectra of Pd $3d_{5/2}$ for synthesised zirconolite samples (a) $x = 0.10$, (b) $x = 0.15$, (c) $x = 0.20$.

Standard spectra for Pr_6O_{11} are shown and overlaid for comparison (red curve).

4 Conclusions

In the present work, the phase assemblage and microstructure of $\text{Ca}_{1-x}\text{Pr}_x\text{ZrTi}_{2-5x/3}\text{Al}_{5x/3}\text{O}_7$ ceramics fabricated by a conventional solid state synthesis route, from mixed oxide precursors, was systematically investigated, with Pr included as a representative surrogate for Np. Synthesis in air at 1350°C produced a phase assemblage comprised of zirconolite-2M (> 93 wt. %) and a secondary perovskite phase at all levels of targeted Pr concentration. Zirconolite was confirmed to adopt the 2M crystal structure by HRTEM and SAED analysis, which is favourable considering the high radiation tolerance and aqueous durability of this phase ^[27]. Analysis of XPS spectra was consistent with the oxidation state of Pr remaining consistent throughout the phase evolution. SEM analyses revealed all specimens sintered with a comparatively dense morphology. The work presented within demonstrate that incorporation of Np within zirconolite may be a feasible route towards disposition, through analogy with the surrogate Pr solid solution, in the compositional range $0.05 \leq x \leq 0.20$.

5 Acknowledgements

LRB, NCH, SKS and LJG are grateful for financial support from the Nuclear Decommissioning Authority and EPSRC (No. EP/P013600/1, EP/S01019X/1, EP/R511754/1 and EP/T011424/1). This work was financially supported by Pearl River Nova Program of Guangzhou (No. 201710010142), State Key Laboratory for Modification of Chemical Fibers and Polymer Materials, Donghua University (No.19ZK0113), National Natural Science Foundation of China (No. 51402055, 51602060, 51832002 and U1401247), and Guangdong Innovative and Entrepreneurial Research Team Program (No. 2013G061 and 2014YT02C49).

6 Declaration of Competing Interest

The authors declare that they have no known competing financial interests or personal relationships that could have appeared to influence the work reported in this paper.

7 References

- [1] W. M. Stacey, *Nuclear Reactor Physics*, second ed., Wiley-VCH Verlag GmbH & Co. KGaA, Weinheim, Germany, 2007.
- [2] I. W. Donald, *Waste Immobilization in Glass and Ceramic Based Hosts*, John Wiley & Sons, Ltd., Chichester, United Kingdom, 2010.
- [3] M. I. Ojovan, W. E. Lee, *Introduction to Nuclear Waste Immobilisation*, Elsevier Science Publishers, Amsterdam, Netherlands, 2005.
- [4] Z. Yoshida, S. G. Johnson, T. Kimura, J. R. Krsul, Neptunium, in: L. R. Morss, N. M. Edelstein, J. Fuger (Eds.) *The Chemistry of the Actinide and Transactinide Elements*, Springer Netherlands, Dordrecht, 2006, pp. 699–812. https://doi.org/10.1007/1-4020-3598-5_6.
- [5] S. Nakayama, Y. Iida, T. Nagano, T. Akimoto, Leaching behavior of a simulated bituminized radioactive waste form under deep geological conditions, *J. Nucl. Sci. Technol.* 40 (2003) 227–237. <https://doi.org/10.1080/18811248.2003.9715353>.
- [6] S. Wang, E. V. Alekseev, J. Ling, S. Skanthakumar, L. Soderholm, W. Depmeier, T. E. Albrecht-Schmitt, Neptunium diverges sharply from uranium and plutonium in crystalline borate matrixes: insights into the complex behavior of the early actinides relevant to nuclear waste storage, *Angew. Chem., Int. Ed.* 49

(2010) 1263–1266. <https://doi.org/10.1002/anie.200906127>.

- [7] H. Kinoshita, K. Kuramoto, M. Uno, S. Yamanaka, H. Mitamura, T. Banba, Mechanical integrity of yttria-stabilised zirconia doped with Np oxide, *Mater. Res. Soc. Symp. Proc.* 932 (2006) 52. <https://doi.org/10.1557/proc-932-52.1>.
- [8] R. C. Ewing, Ceramic matrices for plutonium disposition, *Prog. Nucl. Energy* 49 (2007) 635–643. <https://doi.org/10.1016/j.pnucene.2007.02.003>.
- [9] A. E. Ringwood, V. M. Oversby, S. E. Kesson, W. Sinclair, N. Ware, W. Hibberson, A. Major, Immobilization of high-level nuclear reactor wastes in SYNROC: a current appraisal, *Nucl. Chem. Waste Manage.* 2 (1981) 287–305. [https://doi.org/10.1016/0191-815x\(81\)90055-3](https://doi.org/10.1016/0191-815x(81)90055-3).
- [10] W. E. Lee, M. I. Ojovan, M. C. Stennett, N. C. Hyatt, Immobilisation of radioactive waste in glasses, glass composite materials and ceramics, *Adv. Appl. Ceram.* 105 (2006) 3–12. <https://doi.org/10.1179/174367606x81669>.
- [11] E. R. Vance, C. J. Ball, R. A. Day, K. L. Smith, M. G. Blackford, B. D. Begg, P. J. Angel, Actinide and rare earth incorporation into zirconolite, *J. Alloys Compd.* 213–214 (1994) 406–409. [https://doi.org/10.1016/0925-8388\(94\)90945-8](https://doi.org/10.1016/0925-8388(94)90945-8).
- [12] D. J. Bailey, S. M. Lawson, S. K. Sun, M. C. Stennett, T. H. Lee, B. Ravel, C. L. Corkhill, J. Heo, N. C. Hyatt, A new approach to the immobilisation of technetium and transuranics: co-disposal in a zirconolite ceramic matrix, *J. Nucl. Mater.* 528 (2020) 151885. <https://doi.org/10.1016/j.jnucmat.2019.151885>.
- [13] R. Gieré, J. Malmström, E. Reusser, G. R. Lumpkin, M. Düggelin, D. Mathys, R. Guggenheim, D. Günther, Durability of zirconolite in hydrothermal fluids: implications for nuclear waste disposal, *Mater. Res. Soc. Symp. Proc.* 663 (2000) 267. <https://doi.org/10.1557/proc-663-267>.
- [14] G. R. Lumpkin, B. D. Begg, K. L. Smith, Radiation damage effects in pyrochlore and zirconolite ceramic matrices for the immobilization of actinide-rich wastes (2000), in: *Scientific Research on the Back-end of the Fuel Cycle for the 21 Century*, Avignon, France, 2000, pp. 575-584.
- [15] E. R. Vance, G. R. Lumpkin, M. L. Carter, D. J. Cassidy, C. J. Ball, R. A. Day, B. D. Begg, Incorporation of uranium in zirconolite ($\text{CaZrTi}_2\text{O}_7$), *J. Am. Ceram. Soc.* 85 (2002) 1853–1859. <https://doi.org/10.1111/j.1151-2916.2002.tb00364.x>.
- [16] B. D. Begg, E. R. Vance, S. D. Conradson, The incorporation of plutonium and neptunium in zirconolite and perovskite, *J. Alloys Compd.* 271–273 (1998) 221–226. [https://doi.org/10.1016/S0925-8388\(98\)00058-9](https://doi.org/10.1016/S0925-8388(98)00058-9).

- [17] B. D. Begg, E. R. Vance, R. A. Day, M. Hambley, S. D. Conradson, Plutonium and neptunium incorporation in zirconolite, *Mater. Res. Soc. Symp. Proc.* 465 (1996) 325. <https://doi.org/10.1557/proc-465-325>.
- [18] E. R. Vance, C. J. Ball, M. G. Blackford, D. J. Cassidy, K. L. Smith, Crystallisation of zirconolite from an alkoxide precursor, *J. Nucl. Mater.* 175 (1990) 58–66. [https://doi.org/10.1016/0022-3115\(90\)90270-w](https://doi.org/10.1016/0022-3115(90)90270-w).
- [19] P. Zeng, Y. Teng, Y. Huang, L. Wu, X. Wang, Synthesis, phase structure and microstructure of monazite-type $Ce_{1-x}Pr_xPO_4$ solid solutions for immobilization of minor actinide neptunium, *J. Nucl. Mater.* 452 (2014) 407–413. <https://doi.org/10.1016/j.jnucmat.2014.05.068>.
- [20] R. Shannon, Revised effective ionic radii and systematic studies of interatomic distances in halides and chalcogenides, *Acta Crystallogr., Sect. A* 32 (1976) 751–767. <https://doi.org/10.1107/S0567739476001551>.
- [21] B. Toby, EXPGUI, a graphical user interface for GSAS, *J. Appl. Crystallogr.* 34 (2001) 210–213. <https://doi.org/10.1107/S0021889801002242>.
- [22] K. R. Whittle, N. C. Hyatt, K. L. Smith, I. Margiolaki, F. J. Berry, K. S. Knight, G. R. Lumpkin, Combined neutron and X-ray diffraction determination of disorder in doped zirconolite-2M, *Am. Mineral.* 97 (2012) 291–298. <https://doi.org/10.2138/am.2012.3848>.
- [23] M. Jafar, P. Sengupta, S. N. Achary, A. K. Tyagi, Phase evolution and microstructural studies in $CaZrTi_2O_7-Nd_2Ti_2O_7$ system, *J. Am. Ceram. Soc.* 97 (2014) 609–616. <https://doi.org/10.1111/jace.12664>.
- [24] L. R. Blackburn, S. Sun, L. J. Gardner, E. R. Maddrell, M. C. Stennett, N. C. Hyatt, A systematic investigation of the phase assemblage and microstructure of the zirconolite $CaZr_{1-x}Ce_xTi_2O_7$ system, *J. Nucl. Mater.* 535 (2020) 152137. <https://doi.org/10.1016/j.jnucmat.2020.152137>.
- [25] S. Ji, M. Su, C. Liao, S. Ma, Z. Wang, K. Shih, C. -K. Chang, J. -F. Lee, T. -S. Chan, Y. Li, Synchrotron x-ray spectroscopy investigation of the $Ca_{1-x}Ln_xZrTi_{2-x}(Al, Fe)_xO_7$ zirconolite ceramics (Ln = La, Nd, Gd, Ho, Yb), *J. Am. Ceram. Soc.* 103 (2020) 1463–1475. <https://doi.org/10.1111/jace.16832>.
- [26] C. -Z. Liao, K. Shih, W. E. Lee, Crystal structures of Al–Nd codoped zirconolite derived from glass matrix and powder Sintering, *Inorg. Chem.* 54 (2015) 7353–7361. <https://doi.org/10.1021/acs.inorgchem.5b00847>.
- [27] P. J. McGlenn, K. P. Hart, E. H. Loi, E. R. Vance, pH dependence of the aqueous dissolution rates of

perovskite and zirconolite at 90°C, *Mater. Res. Soc. Symp. Proc.* 353 (1994) 847.
<https://doi.org/10.1557proc-353-847>.

[28] D. Wolframm, M. Ratzke, M. Kappa, M. J. Montenegro, M. Döbeli, T. Lippert, J. Reif, Pulsed laser deposition of thin Pr_xO_y films on Si(100), *Mater. Sci. Eng. B* 109 (2004) 24–29.
<https://doi.org/10.1016/j.mseb.2003.10.022>.

[29] F. H. Aragón, I. Gonzalez, J. A. H. Coaquira, P. Hidalgo, H. F. Brito, J. D. Ardisson, W. A. A. Macedo, P. C. Morais, Structural and surface study of praseodymium-doped SnO_2 nanoparticles prepared by the polymeric precursor method, *J. Phys. Chem. C* 119 (2015) 8711–8717.
<https://doi.org/10.1021/acs.jpcc.5b00761>.

[30] S. Lütkehoff, M. Neumann, A. Ślebarski, 3d and 4d x-ray-photoelectron spectra of Pr under gradual oxidation, *Phys. Rev. B* 52 (1995) 13808–13811. <https://doi.org/10.1103/physrevb.52.13808>.

[31] L. M. Mottram, S. Cafferkey, A. R. Mason, T. Oulton, S. -K Sun, D. J. Bailey, M. C. Stennett, N. C. Hyatt, A feasibility investigation of speciation by Fe K-edge XANES using a laboratory X-ray absorption spectrometer, *J. Geosci.* 65 (2020) 27–35. <https://doi.org/10.3190/jgeosci.299>.

[32] H. Fujishiro, T. Naito, S. Ogawa, N. Yoshida, K. Nitta, J. Hejtmánek, K. Knížek, Z. Jiráček, Valence shift of Pr ion from 3+ to 4+ in $(\text{Pr}_{1-y}\text{Y}_y)_{0.7}\text{Ca}_{0.3}\text{CoO}_3$ estimated by X-Ray absorption spectroscopy, *J. Phys. Soc. Jpn.* 81 (2012) 064709. <https://doi.org/10.1143/jpst.81.064709>.

[33] J. Dumschat, G. Wortmann, I. Felner, $L_{II,III}$ near-edge study of tetravalent Pr-oxides: PrBaO_3 and PrO_2 , *Phys. Rev. B: Condens. Matter Mater. Phys.*, 208–209 (1995) 313–315. [https://doi.org/10.1016/0921-4526\(94\)00685-o](https://doi.org/10.1016/0921-4526(94)00685-o).

Caption

Fig. 1) Powder XRD data for $\text{Ca}_{1-x}\text{Pr}_x\text{ZrTi}_{2-5x/3}\text{Al}_{5x/3}\text{O}_7$ at $x =$ (a) 0.05 , (b) 0.10 , (c) 0.15 and (d) 0.20 compositions sintered in air at 1350 °C for 20 h. Green labels and black vertical lines are representative of the theoretical intensities and the Bragg positions of zirconolite-2M reflections (ICSD: 190015 ^[22]).

Fig. 2) SAED patterns for $\text{Ca}_{1-x}\text{Pr}_x\text{ZrTi}_{2-5x/3}\text{Al}_{5x/3}\text{O}_7$ taken along the $[14\bar{2}]$ and $[010]$ zone axis of $x = 0.05$ (**Fig. 2a-b**); $[14\bar{2}]$ and $[110]$ zone axes of $x = 0.15$ (**Fig. 2c-d**).

Fig. 3) HRTEM images of $\text{Ca}_{1-x}\text{Pr}_x\text{ZrTi}_{2-5x/3}\text{Al}_{5x/3}\text{O}_7$ with corresponding SAED at $x =$ (a) 0.05 and (b) 0.15.

Fig. 4) Representative BSE micrographs of the $\text{Ca}_{1-x}\text{Pr}_x\text{ZrTi}_{2-5x/3}\text{Al}_{5x/3}\text{O}_7$ ceramic microstructure at $x =$ (a) 0.05, (b) 0.10, (c) 0.15 and (d) 0.20, after sintering in air at 1350 °C for 20 h. Red circles highlight the CaTiO_3 phase. The black region in grain boundary is the porosity.

Fig. 5) Representative BSE micrograph and corresponding EDS data mapping for the $x = 0.20$ sample. The red circles highlight the CaTiO_3 phase.

Fig. 6) XPS spectra of Pd $3d_{5/2}$ for synthesised zirconolite samples (a) $x = 0.10$, (b) $x = 0.15$, (c) $x = 0.20$. Standard spectra for Pr_6O_{11} are shown and overlaid for comparison (red curve).

Table 1) Weight fraction of the zirconolite-2M phase and relative density of obtained product, alongside comparison of nominal and measured $\text{Ca}_{1-x}\text{Pr}_x\text{ZrTi}_{2-5x/3}\text{Al}_{5x/3}\text{O}_7$ compositions determined by EDS analysis. # - Data are calculated based on only cations and normalised.